Title

Printed Strain Sensors Using Graphene Nanosheets Prepared by Water-Assisted Liquid Phase Exfoliation

Journal

Advanced Materials Interfaces, 6(9)

ISSN

2196-7350

Authors

Manna, Kausik
Wang, Long
Loh, Kenneth J
et al.

Publication Date

2019-05-01

DOI

10.1002/admi.201900034

Peer reviewed

DOI: 10.1002/((please add manuscript number))
Article type: Communication

Printed Strain Sensors using Graphene Nanosheets Prepared by Water-Assisted Liquid Phase Exfoliation

Kausik Manna, Long Wang, Kenneth J. Loh, and Wei-Hung Chiang**

Kausik Manna, Wei-Hung Chiang*
Department of Chemical Engineering, National Taiwan University of Science and Technology, Taipei 10607, Taiwan
*Co-Corresponding Author E-mail: whchiang@mail.ntust.edu.tw

Long Wang, Kenneth J. Loh*
Department of Structural Engineering, University of California-San Diego, La Jolla, CA, 92093, USA
*Co-Corresponding Author E-mail: kenloh@ucsd.edu

Keywords: liquid phase exfoliation, graphene nanosheet, strain sensor, thin film

The scalable production of graphene nanosheets (GNS) at high quality is a critical milestone for various potential applications, including sensors[1], biosensors[2-4], nanoelectronics[5], nanocomposites[6], energy conversion and storage[7, 8], catalysis[9], and biomedical applications[10]. Among those applications, strain sensing is critically important in the context of structural health monitoring, since various types of damage (*e.g.*, fatigue, cracks, impacts, and delamination, among others) can be detected and assessed based on strain measurements. As compared to conventional bulky and discrete strain sensors (*e.g.*, foil strain gages and fiber optics), nanostructured materials are promising candidates for fabricating novel, highly sensitive, and flexible thin film-based strain sensors that can be deposited over large structural surfaces[1, 11]. While strain sensors based on zinc oxide[12, 13], carbon nanotubes (CNT)[14, 15], and metal nanowires[16, 17] have been proposed, GNS provides

tremendous opportunities for improving the properties of next-generation strain sensors[1, 11], in particular, by leveraging their nanostructured two-dimensional (2D) morphology and extraordinary mechanical and electrical properties[6, 18, 19].

Over the last decade, various methods have been introduced for the synthesis of GNS, including micromechanical exfoliation[20], chemical vapor deposition (CVD)[21], electrochemical exfoliation[22-24], the reduction of graphene oxide (GO)[25], and liquid-phase exfoliation (LPE) of bulk graphite in various solvents[26]. Although the bulk production of GNS by reduction of GO is a popular method[25, 27], the drastic conditions (*i.e.*, the use of strong reducing agents or high temperatures) involved in the reduction process often introduce impurities or defects in the reduced GO (RGO), which affect the intrinsic properties of GNS. In addition, the synthesis of RGO chemically or thermally is time-consuming, laborious, and hazardous for the environment. While CVD is capable of producing almost defect-free GNS, the yield is low in terms of bulk production. In contrast, LPE of bulk graphite via sonication in various solvents[28, 29] to prepare GNS has attracted considerable attention due to its simple operations, low defects in the produced nanosheets, and minimal environmental impact[30].

Recently, mixtures of solvents have been demonstrated as successful liquid phases to improve the yield and quality of GNS, as well as other (2DLMs) in LPE[31],[29]. The successful employment of N-methylpyrrolidinone (NMP) for liquid phase exfoliation of LMs have opened new directions in the synthesis and applications of 2DLMs[26, 32]. However, the defects generated in GNS during ultrasonication with NMP[33] degrade their quality and affect its intrinsic properies and, consequently, its applications. Exploring new solvents for LPE to obtain high yields of stable and high quality GNS remains essential. A previous study has shown that the stability of RGO dispersion can be significantly enhanced by adding a small amount of water to NMP [34]. Moreover, some recent studies [29, 35-37] have demonstrated how trace amounts of water in an NMP-water mixed solvent system improve the solvent quality

for LPE of LMs. Briefly, the presence of water plays an important role in solid-solvent interactions and stability of the dispersion of exfoliated nanosheets of LMs [37].

In this work, we report the effect of water as the co-solvent with NMP in LPE for improving the yield and quality of GNS while demonstrating how high-quality GNS can lead to higher performance paper-based graphene strain sensors. First, we synthesized low-defect few-layer GNS from graphite using a surfactant-free, efficient, and economical LPE process [29] by using a water-NMP mixed solvent. Second, we fabricated strain sensors by preparing an aqueous GNS dispersion and directly depositing it on paper. In short, using the high-quality GNS prepared by water-assisted LPE (denoted as LPEGNS for the remainder of this article), their material properties were successfully translated to the bulk-scale, and the flexible graphene paper specimens exhibited improvements in electrical properties and piezoresistivity as compared to RGO-based sensors. In addition, this study also showed that the electrical conductivity and strain sensing performance of LPEGNS strain sensors could be further improved through post-fabrication thermal annealing. These results show promise for developing low-cost, flexible, and highly-sensitive GNS-based strain sensors.

Figure 1 illustrates an overview of the experimental procedure employed for LPEGNS preparation, paper-based strain sensor fabrication, and strain sensing tests. First, LPEGNS was prepared from bulk graphite powder using a surfactant-free LPE technique[29], with water as the co-solvent with NMP (**Figure 1a**). To highlight the advantage of using LPEGNS for stain sensing, RGO nanosheets were also synthesized and used to fabricate strain sensors, and the results were compared. RGO was prepared using a combination of modified Hummers' method[38] and thermal reduction. The detailed procedures of LPEGNS[29] and RGO preparations are described in the **Experimental Section**. The step-by-step fabrication of paper-based graphene (LPEGNS and RGO) strain sensors is exhibited in **Figure 1b**. In short, aqueous graphene suspensions prepared by ultrasonicating GNS in

polyoxyethylene(40)nonylphenyl ether (IGEPAL® CO890) were directly deposited onto standard printer paper. Then, air-dried graphene paper was cut to obtain smaller specimens onto which conductive electrodes were established for measurement purposes. One can observe from the photograph of fabricated sensors (**Figure 1b-5**) that LPEGNS and RGO were uniformly distributed and were well-integrated with paper fibers, and the incorporation of GNS did not compromise the flexibility of the pristine substrate (inset of **Figure 1b-5**). In this study, a cantilevered beam (**Figure 1c-1**) was used to compare the electromechanical performance of the RGO-based and LPEGNS-based sensors, while three-point-bending tests (**Figure 1c-2**) were conducted to further characterize their strain sensing response.

The representative ultraviolet-visible (UV-vis) absorption spectra of LPEGNS dispersions prepared with varying water mass fractions (m_w) exhibit a peak at 266 nm (**Figure 2a**), which is consistent with previous reports[26, 31] and show no major alteration or oxidations in the LPEGNS structures during exfoliation[26]. The photographs of LPEGNS dispersions as a function of m_w are presented in **Figure S1** (Supporting Information). The optimal m_w for exfoliation of graphite and the exfoliated concentration were evaluated by a systematic UV-vis spectroscopic study of the LPEGNS dispersions at different m_w (**Figure 2b**), and the absorption coefficient and exfoliated concentration of LPEGNS was evaluated at 660 nm by the filtration and weighing method (detailed in the **Section S1**, Supporting Information)[26]. **Figure 2b** indicates that the exfoliated concentrations of LPEGNS increased initially with the increase of m_w, and optimal m_w was found to be 0.2 – 0.3. In this study, the LPEGNS obtained at m_w = 0 and m_w = 0.2 have been distinguished as LPEGNS-1 and LPEGNS-2, respectively. The final concentration of LPEGNS-2 obtained after centrifugation was 0.43 mg mL^{-1}, which was almost 2.5 times that of LPEGNS-1 (**Figure 2b**). The stability of the LPEGNS-2 dispersion was further examined by UV-vis. **Figure 2c** shows a representative photograph of the LPEGNS-2 dispersion after 18 months showing Tyndall effect, and **Figure**

2d shows the stability of the LPEGNS-2 dispersion as a function of time, indicating that the LPEGNS-2 dispersion remained stable even after 18 months. The high yield and exceptional stability of LPEGNS-2 dispersion may be attributed to the favorable graphite-water/NMP interactions and stabilization of exfoliated nanosheets by water-NMP heteroassociation (**Section S4, Figures S7** and **S8**, supporting information) [37].

Micro-Raman spectroscopic analysis was performed to study the defect densities of LPEGNS and RGO. The defect analysis by Raman spectroscopy is thoroughly discussed in **Section S2** (Supporting Information). Both LPEGNS-1 and LPEGNS-2 showed three typical peaks assigned as D, G, and 2D peaks at 1340, 1577, and 2692 cm^{-1}, respectively (**Figure 2e**), which are consistent with previous reports[26, 39]. The D and G bands are due to structural imperfections in the carbon basal plane[40] (or topological defects[41]) along the edges and sp^2 carbon bond stretching of the E_{2g} mode[40], respectively. The 2D peak is the overtone of the D peak and is typically used to estimate the number of layers in graphene[42]. The shapes and positions of the 2D peaks of LPEGNS-1 and LPEGNS-2 samples suggested single- and few-layer graphene structures[42].

In general, the defect densities of graphitic materials can be estimated from the intensity ratio of the D to G peaks [I(D)/I(G)][43]. The estimated I(D)/I(G) values for LPEGNS and RGO are summarized in **Table S1** in Supporting Information. The average I(D)/I(G) was found to be 0.68 and 0.51 for LPEGNS-1 and LPEGNS-2 respectively, thereby indicating that the addition of optimal amounts of water reduced the defect densities in LPEGNS-2. According to previous studies,[41] the I(D)/I(G) values for graphite is between 0.2 to 0.7, which implies that LPE by sonication in a water-NMP solvent system led to negligible defects in LPEGNS-2 as compared to defects caused by oxidation (average I(D)/I(G) $\approx$ 1)[41, 44]. Moreover, in all the cases, the I(D)/I(D') values (**Table S1**) remain less than 4.5, implying that the defects in the as-produced graphene nanosheets mainly existed along the edges, thereby

excluding vacancies and sp^3 type defects[41, 45]. In contrast, RGO shows a I(D)/I(G) value around ~ 1.08, indicating the presence of higher defect densities caused by oxidation (**Figure 2e**). **Figure 2f** clearly shows that a larger I(D)/I(G) corresponds to a larger full-width half-maximum of the G peak FWHM(G), which indicates that a larger defect density corresponds to higher FWHM(G), and these results are also consistent with previous reports[33]. The correlation between I(D)/I(G) and FWHM(G) were also used to evaluate defect densities in GNS[33], where the lower values of I(D)/I(G) and FWHM(G) of LPEGNS-2 indicated that the water-NMP co-solvent (m_w = 0.2) approach caused fewer defects to LPEGNS during sonication as compared to using pure NMP (**Figure 2f**). The Raman I(D)/I(D') analysis (**Table S1**) demonstrated that the defects generated in LPEGNS during the exfoliation process were mainly edges or topological defects by nature, rather than oxidative defects[41]. The defects in LPEGNS were also estimated from the chemical purity and C/O ratio by X-ray photoelectron spectroscopy (XPS) analyses (**Figure S2, S3b,** and **S3d** in the Supporting Information). The absence of any oxidized carbon in the exfoliated graphene layers was also supported by XPS analysis. The C/O ratio of LPEGNS were estimated as a function of m_w and is presented in **Table S2** and **Figure S3 b, d** . The C/O ratio of LPEGNS-2 was found to be 29.96 which is appreciably higher than the previously reported C/O ratio (6.95 to 21.11) of graphene nanosheets produced by various reduction methods of graphene oxide [46-53]. The high C/O ratio of LPEGNS-2 clearly suggests that oxidation did not take place on the graphitic structure during exfoliation. The trace amount of oxygen observed in XPS wide scan spectra (**Figure S2b**) of both LPEGNS-2 and bulk graphite powder might have appeared due to exposure to air[54, 55] (**Section S3** in Supporting Information).

Extensive transmission electron microscope (TEM) measurements were performed to determine the morphology of exfoliated LPEGNS-2, as shown in **Figs. 2g** and **S3**. The statistical size analysis of LPEGNS-2 from TEM images revealed that the majority of the

exfoliated LPEGNS-2 are characterized by a lateral dimension of ~ 0.5 – 2.0 μm (**Figure S4**). The number of layers in LPEGNS-2 were estimated from high-resolution TEM (HRTEM) images by carefully observing the edges of the nanosheets[26] (**Figure S3c**), where mono-layer and few-layer structures were observed in LPEGNS-2, which is consistent with Raman analysis. The thickness of the LPEGNS-2 was also analyzed by atomic force microscopy (AFM). AFM image of graphene (**Figure S6**) show small nanosheets of LPEGNS-2 with a thickness of 2 – 4 nm, suggesting few (4 – 8) layered nanosheets. HRTEM and corresponding fast Fourier transform (FFT) images (**Figures 2h** and **S3d**) show the hexagonal regular crystalline structure of LPEGNS-2, suggesting no severe distortions in crystallinity[26]. In contrast, TEM images of RGO (**Figure 2i**) clearly exhibit hole-like defects introduced by the chemical modification that occurred during its preparation.

To demonstrate the importance of using high-quality GNS to obtain enhanced bulk materials with favorable performance attributes, thin film strain sensors were fabricated and tested. **Figs. 3a** and **3b** show the representative nominal resistance time histories of RGO-CO890 and LPEGNS-2-CO890 paper sensors, respectively; the plots also include their average unstrained resistance values and standard deviations. It was found that samples fabricated with RGO possessed significantly higher resistance than their LPEGNS-based counterparts. The inferior bulk electrical conductivity of RGO-based sensors could be mainly attributed to the structural defects in the nanosheets that were inevitably introduced when removing the oxygen-containing groups (**Figure 2h**). Furthermore, upon closer examination of the resistance time histories over a period of 500 s (insets of **Figures 3a** and **3b**), RGO-CO890 paper sensors exhibited a higher noise floor. Here, the root-mean-square (RMS) noise (R_{RMS}) of the nominal resistance data were calculated using **Equation 1**,

$$R_{RMS} = \sqrt{\frac{1}{n}\sum_{i=1}^{n}(R_i(t) - R_{ave})^2} \quad (1)$$

where R_i represents the measured resistance data as a function of time (t), whose average is denoted by R_{ave}, and n is the total number of measurements included. It should be mentioned that R_{ave} is also regarded as the nanocomposite's unstrained nominal resistance. The calculated RMS noise values for the two sample sets tested are listed in **Figs. 3a** and **3b**, which confirmed that the RGO-CO890 sensors were characterized by significantly higher noise. It is hypothesized that RGO-CO890 graphene paper nanocomposites contained unstable or defective conductive pathways, which could be more susceptible to external stimuli (*e.g.*, changes in ambient temperature, humidity, and light), resulting in considerable variations (or noise) in their electrical resistivity.

The strain sensing performance of RGO and LPEGNS was also compared. **Figs. 3c** and **3d** show the resistance changes of RGO- and LPEGNS-2-based samples when subjected to applied strains, respectively. The electromechanical response of RGO-CO890 samples could be barely detected because of the dominant effects of noise during applied strains (**Figure 3c**). On the other hand, one can observe from **Figure 3d** that the resistance of LPEGNS-2-based sensors increased in tandem with increasingly applied tensile strains and without any phase lag. During the unloading process, the paper sensors' resistance decreased simultaneously and returned to their initial unloaded resistance. The piezoresistivity of graphene paper could be primarily contributed by the disturbance of electrically conductive pathways in the nanocomposite under applied strains. In particular, portions of deposited GNS could experience strain-induced rigid-body motion (along with the paper fibers) to become physically and electrically disconnected (during applied tensile strains), which would disrupt the originally formed conductive network and impede electrical current flow. As a result, the bulk electrical resistance of the nanocomposite would increase correspondingly. When tensile strains were removed, the paper fibers restored to their previous configurations, enabling LPEGNS-2 to re-establish the initial percolation network, reducing bulk film resistance to its

initial value. The assumption of elastic behavior of paper is valid given that only small strains were applied and that no residual strains (or permanent deformation) were observed after the tests. However, for RGO-based specimens, since the conductive network itself was unstable and that RGO was sensitive to ambient effects, the nanocomposite's piezoresistivity was unreliable, if detectable at all. Therefore, the superior quality of LPEGNS-2 versus RGO is crucial for manufacturing paper-based thin films with favorable strain sensing properties.

In addition, the electrical and electromechanical properties of LPEGNS-2-CO890 paper sensors were further characterized and improved. Here, the specimens were fabricated in a more controlled manner by using a syringe to deposit a controlled amount of solution onto paper. The process was repeated to deposit multiple thin layers of LPEGNS-2-CO890 film. Moreover, samples were also thermally annealed after being air-dried at room temperature. **Figure 4a** presents the nominal resistance of a representative sample set before and after annealing. As more layers of LPEGNS-2-CO890 film were deposited, the resistance of the non-annealed specimens decreased accordingly, and it tended to plateau when large numbers of layers were fabricated. This result indicates that the electrical conductivity of the LPEGNS-2-based paper sensors can be readily tuned by controlling the number of deposition cycles performed. Besides, post-fabrication annealing was able to ubiquitously enhance the conductivity of all samples, yielding ~ 23% decrease in their nominal resistance, regardless of the number of layers deposited. It was assumed that annealing could remove residual water and ethanol molecules that would otherwise be trapped in the nanocomposite post-fabrication. Therefore, annealing could improve LPEGNS-to-LPEGNS contacts, thereby forming a more integrated network with increased electrically conductive pathways and reduced contact impedance.

Furthermore, to investigate the electromechanical performance of LPEGNS-2-CO890 paper sensors, they were subjected to three-point-bending tests (**Figure 1c-2**). **Figure 4b**

shows the change in resistance of a representative annealed specimen subjected to applied strains; similar strain sensing response was observed for non-annealed samples, as is shown in **Figure S9**. It was confirmed that LPEGNS-2-CO890 paper sensors possessed stable, reversible, and repeatable piezoresistivity.

This study also characterized the strain sensitivity or gage factor (GF) of the graphene paper sensors from the measured resistance and applied strain time histories using **Equation 2**[56],

$$GF = \frac{R_n}{\Delta\varepsilon} = \frac{\Delta R / R_{ave}}{\Delta\varepsilon} \tag{2}$$

where R_n represents normalized change in resistance, which is computed using the specimen's change in resistance (ΔR) with respect to its nominal resistance when strain ($\Delta\varepsilon$) was applied. **Figure 4c** plots R_n of representative 14- and 30-layer samples as a function of applied tensile strains. One can observe an approximately exponential resistance changing trend, which indicates that strain transfer in the conductive networks of the nanocomposite might depend on strain levels. In particular, at higher strain level, tensile strains could more effectively be transferred in the nanocomposite to induce more significant changes in its bulk resistance. However, in order to evaluate GF, their normalized resistance change versus strain raw data was fitted with a linear function, considering only data for which applied strains were larger than 25% of value of applied peak strain; the fitted least-squares regression lines are shown in **Figure 4c**. The average GFs and their standard deviations of non-annealed and annealed sample sets are summarized in **Figure 4d**. Although GFs of the non-annealed samples did not show strong dependency with respect to the number of layers, those of the annealed films were found to increase as more layers were deposited (except the anomaly of the 26-layer case, which was attributed to experimental error). In addition, annealing was able to improve the GFs for samples that included more than 14 layers. It is hypothesized that, by releasing

trapped water and ethanol molecules during annealing, strains could be more effectively transferred to the GNS network and cause more significant changes to the configuration of the conductive pathways. Moreover, since nominal resistance (*i.e.*, R_{ave}) of the paper sensors decreased after annealing (*i.e.*, the denominator in **Equation 2** became smaller), the same amount of strain-induced resistance change would result in higher GF for annealed samples.

This study also investigated the potential of using the proposed method for fabricating GNS-paper sensors with different and more complicated geometrical patterns. **Figure S10** shows three different coil patterns created by selectively depositing the GNS-based solution on paper. Here, the line width was 2 mm, and each pattern was formed by depositing 8 layers of film. It can be seen that the deposition was uniform throughout the entire pattern. The ability to fabricate different and complex patterns suggest that this technique can be used for designing and creating nanocomposite thin films suitable for being used, for example, aspassive radio frequency identification (RFID) antennas. It is anticipated that inkjet printing or other solution-based casting techniques can be further employed to autonomously deposit GNS-based solutions to create these patterns.

In situ Raman spectroscopy of LPEGNS-2-CO890 at variable strain was performed to examine the effects of strain on the hexagonal graphene layers (**Figures 5a, 5b,** and **S11)**. **Figure 5a** clearly shows that there is a shift in the G mode frequency of LPEGNS-2 under applied strain. An LPEGNS-2 film on paper substrate is sufficiently sensitive to respond to small strain (0.02 %), which also implies the high quality (low-defect) of LPEGNS. Despite its irregular trend, the G mode shows an overall blue-shift over the entire strained graphene. The irregularity might be due to the nonuniform strain distribution over the LPEGNS-2 layers. This nonuniformity could be attributed to the consequence of van der Waals interactions between the paper substrate with graphene nanosheets[57]. On the other hand, an overall decreasing trend is observed in the I_D/I_G profile with increasing strain **(Figure 5b)**, which implies that applied strain does not introduce defects or deformations in graphene layers. The

effect of strain on LPEGNS was also investigated by scanning electron microscope (SEM) measurements (**Figure 5c, 5f**). It is noted that no significant deformation due to strain could be observed in SEM images at both high (**Figure 5d, 5f**) and low magnifications (**Figure 5c, 5e**).

In summary, we have demonstrated the low-cost preparation of GNS-based paper strain sensors by leveraging the superior quality of GNS, which were produced through scalable and surfactant-free liquid exfoliation of graphite powders in a water-NMP co-solvent system. The proposed LPE process enabled the enhancement of exfoliation yield (8.6%). Dispersions of as-exfoliated LPEGNS remained stable for up to 18 months, even at high concentrations (0.43 mg mL^{-1}). Furthermore, the exfoliation process also reduced defect densities in GNS. To assess the benefits of different GNS and how these material properties translated to larger length-scales, strain sensing validation tests were conducted. The LPEGNS-based strain sensors, fabricated by depositing and drying dispersed aqueous solutions on standard printer paper, exhibited higher electrical conductivity, lower noise floor, and more stable electromechanical response as compared to their RGO-based counterparts. In addition, post-fabrication thermal annealing was capable of improving the electrical and electromechanical properties of the LPEGNS paper sensors. These results pave way for future practical developments and applications of these nanocomposites as strain sensors for structural health monitoring.

Experimental Section

Materials: Graphite (-325 mesh, 99.995 % pure) microcrystalline powders were purchased from Alfa Aesar. N-methylpyrrolidinone (NMP, 99% extra pure) was from Acors Organics. Polyoxyethylene (40) nonylphenyl ether (average Mn ~ 1982, branched) (IGEPAL® CO890)

and ethanol were obtained from Sigma Aldrich and Fisher Scientific, respectively. All chemicals were used as received. Deionized (DI) water was used in all of the experiments.

GNS preparation: **Figure 1a** summarizes the entire experimental method employed for exfoliation of each material. We used the same 14 mL centrifuge tubes throughout the experiments to avoid material loss due to transfer. Here, 50 mg of each material were measured and placed in 14 mL centrifuge tubes with an initial concentration 5 mg mL^{-1} for exfoliation. The materials were bath sonicated (Elma sonic P60H) for 6 h and at a fixed nominal power and frequency of 100 W and 37 kHz, respectively. The positions of each sample tube were interchanged every 30 min to subject the mixtures to uniform power distribution. The water of the bath sonicator was replaced with normal cold water every 30 min to minimize temperature increase during sonication, and temperature was maintained between 27 – 37 ^{o}C. Sample dispersions were left overnight after sonication, followed by centrifugation at 3,000 rpm for 30 min using a Hettich EBA20. The top 75% of the colloidal supernatant was first collected. Then, the supernatant was kept undisturbed for 24 h for further precipitation, if any, and the upper 67% portion of the colloidal supernatant was used for characterization. Every experiment was repeated for five times to obtain statistically representative results and to account for experimental error.

RGO synthesis: In a typical preparation, 0.1 g of natural graphite was suspended in 100 mL of H_2SO_4, followed by stirring, using a magnetic stirrer, at 300 rpm for 2 h until a visually homogeneous black solution formed. Then, $KMnO_4$ of different quantities was slowly added to the solution and further stirred for another 2 h at room temperature. After that, the temperature was gradually raised and then maintained for 2 h in a water bath (IKA-HS7 digital). When the reaction completed, the product was removed from the heat source, allowed to cool to room temperature, and then poured into 350 g of ice containing 5 mL of 35% H_2O_2 (*i.e.*, to prevent precipitation of insoluble MnO_2). The mixtures were then

centrifuged (at 24,500 rpm and for 30 min) to obtain crude solid (Beckman, Avanti J-25). The solid was removed and then bath-sonicated in 60 mL of DI water for 30 min (IKA-HS7 digital). The material was bath-sonicated again by adding 30 mL of HCl, and the dispersion was centrifuged (24,500 rpm and 30 min). Furthermore, the collected solid was removed and then bath-sonicated in 60 mL of ether for 30 min. Purified GO was then obtained by collecting the centrifuged solid. Finally, exfoliation of GO was conducted by heating it (~ 10 ^{o}C min^{-1}) to 1,000 ^{o}C in an inert Ar atmosphere. After thermal reduction, RGO was obtained.

Paper-based strain sensor fabrication: First, 0.5 mg mL^{-1} GNS (RGO and LPEGNS) was added to 0.5 wt% CO890 aqueous solution (**Figure 1b-1**). Here, a water-based solution was preferred over organic solvents (*e.g.*, NMP) so as to avoid damaging the cellulose structure of paper fibers or compromising the mechanical properties of the paper substrates. The mixture was then subjected to 2 h of high-energy probe sonication (3 mm tip, 150 W, 22 kHz) for dispersing GNS (**Figure 1b-2**). Second, using disposable pipettes, 6 mL of GNS-CO890 solution was deposited to cover a 12×2.5 cm^2 rectangular area on paper, as is shown in **Figure 1b-3**. The surface tension of the solution was found sufficient to confine the solution within the rectangular area and, hence, ensured that the amount of GNS deposited in each paper specimen was the same. It should be noted that the deposition was conducted on a horizontal platform, on which the GNS-CO890 solution could be uniformly distributed. After being air-dried at room temperature overnight, the GNS paper was cut to form 14×1 cm^2 specimens (with 1 cm margins on both the longitudinal ends of the specimen), as is shown in **Figure 1b-4**. **Figure 1b-4** also illustrates the technique for establishing electrodes, where copper tape strips were sandwiched between two layers of conductive silver paste so as to minimize contact resistance. Here, the gage length was 30 mm. On the other hand, to improve the ease of fabricating LPEGNS-based samples, ethanol was added to 0.7 mg mL^{-1} LPEGNS-CO890 dispersed solutions (5:1 sonicated solution-to-ethanol by volume), and the mixture was then

subjected to cold bath sonication for 30 min. The fast evaporation of ethanol could accelerate the integration of GNS with the paper fibers. In addition, a syringe was used to deposit the dispersed LPEGNS-CO890/ethanol solution to form 60×2 mm^2 thin rectangular strips on paper. After the samples fully dried, electrodes were attached as shown in **Figure 1b-4**, and the gage length was 20 mm. Moreover, post-fabrication thermal annealing was performed by subjecting the dried LPEGNS-based samples to annealing at 180 ^oC for 1 h in vacuum using a vacuum oven (ADP300C, Yamato Scientific America). It should be noted that all electrical measurements were performed after annealed sample sets cooled down to room temperature overnight.

Strain sensing test setup: A commercial foil strain gage (GF of 2.13 ± 1% at room temperature) was installed on the beam and parallel to the graphene paper sensors using epoxy for measuring induced strains. In contrast, double-sided tape and Kapton tape were employed for affixing the GNS paper sensors onto the test beam, since epoxy might affect the intrinsic electrical properties of these specimens. The interface was strong and reliable enough that no slippage was observed during the tests. However, it should be mentioned that strain transfer by tape should be less effective than epoxy. This also means that the strain sensing results, such as the GF estimates, would be lower and more conservative. Then, quasi-static strain was applied uniformly to both the GNS paper sensor and strain gage by gently placing weights onto the free end of the beam (**Figure 1c-1**). Here, two Keysight 34465A digital multimeters (DMM) were employed to simultaneously measure the electrical resistance of the GNS paper sensor and strain gage. Both DMMs were controlled by a Keysight BenchVue program, which also recorded all the data. To conduct the three-point-bending tests on LPEGNS paper sensors, a Test Resources 150R load frame was employed to apply multiple cycles of compressive loading (max displacement: 2 mm; load rate: 1 mm min^{-1}) at the mid-span of the steel plate (**Figure 1c-2**). The samples and strain gage were affixed onto the

backside (*i.e.*, tension face) of the steel plate. Similarly, two DMMs and the BenchVue software were used for data acquisition.

Material characterization: Ex situ characterization of the starting materials and as-produced samples was performed by absorbance spectroscopy, TEM, XPS, and micro Raman. Absorbance spectra of exfoliated dispersions were recorded using a JASCO V676 UV-Vis-NIR spectrophotometer in an identical pair of quartz cuvette with a path length of 1 cm. Baseline correction was done using corresponding solvents during every spectral measurement. Cold-field emission Cs-corrected TEM (JEOL ARM-200F, Japan) with 200 kV accelerating voltage was used. Carbon-coated copper grids (400 mesh) were used for TEM sample preparation. XPS (VG ESCALAB 250, Thermo Fisher Scientific, UK) was performed using a monochromatic Al Kα X-ray radiation (10 kV and 10 mA). The source power was set to 72 W, and pass energies of 200 eV for survey scans and 50 eV for high-resolution scans were used. Raman scattering studies were performed at room temperature with a JASCO 5100 spectrometer (λ = 533 nm). The thin films for XPS and Raman analysis were prepared on Si wafer and dried in a hot air oven at 60 ^{o}C.

Supporting Information

Experimental details and additional materials analysis. This material is available from the Wiley Online Library or from the author.

Acknowledgements

This work was supported by the Ministry of Science and Technology (MOST) of Taiwan (MOST Grant no. MOST 103-2221-E-011-150-MY2 and MOST 104-2923-E-011-001-MY3). KM acknowledges the receipt of fellowship from MOST of Taiwan. Additional support was also provided by the U.S. National Science Foundation (NSF) under grant number CMMI

CAREER-1253654, the U.S. Office of Naval Research (ONR) under grant number N00014-18-1-2483, and the Jacobs School of Engineering, University of California-San Diego.

Reference

[1] Tian, H.; Shu, Y.; Cui, Y.-L.; Mi, W.-T.; Yang, Y.; Xie, D.; Ren, T.-L., *Nanoscale* **2014,** *6*, 699-705.

[2] Shuai, H.-L.; Huang, K.-J.; Xing, L.-L.; Chen, Y.-X., *Biosens. Bioelectron.* **2016,** *86*, 337-345.

[3] Shuai, H.-L.; Huang, K.-J.; Zhang, W.-J.; Cao, X.; Jia, M.-P., *Sens. Actuators, B* **2017,** *243*, 403-411.

[4] Shuai, H.-L.; Wu, X.; Huang, K.-J., *J. Mater. Chem. B* **2017,** *5*, 5362-5372.

[5] Westervelt, R. M., *Science* **2008,** *320*, 324-325.

[6] Wei, W.; Qu, X., *Small* **2012,** *8*, 2138-2151.

[7] Lee, Y.-H.; Zhang, X.-Q.; Zhang, W.; Chang, M.-T.; Lin, C.-T.; Chang, K.-D.; Yu, Y.-C.; Wang, J. T.-W.; Chang, C.-S.; Li, L.-J.; Lin, T.-W., *Adv. Mater.* **2012,** *24*, 2320-2325.

[8] Zhu, L.; Fu Tan, C.; Gao, M.; Ho, G. W., *Adv. Mater.* **2015,** *27*, 7681-7681.

[9] Luo, B.; Liu, S.; Zhi, L., *Small* **2012,** *8*, 630-646.

[10] Liu, C.-J.; Tai, S.-Y.; Chou, S.-W.; Yu, Y.-C.; Chang, K.-D.; Wang, S.; Chien, F. S.-S.; Lin, J.-Y.; Lin, T.-W., *J. Mater. Chem.* **2012,** *22*, 21057-21064.

[11] Park, J. J.; Hyun, W. J.; Mun, S. C.; Park, Y. T.; Park, O. O., *ACS Appl. Mater. Interfaces* **2015,** *7*, 6317-6324.

[12] Wang, Z. L.; Song, J., *Science* **2006,** *312*, 242-246.

[13] Zhou, J.; Gu, Y.; Fei, P.; Mai, W.; Gao, Y.; Yang, R.; Bao, G.; Wang, Z. L., *Nano Lett.* **2008,** *8*, 3035-3040.

[14] Li, Y.; Shang, Y.; He, X.; Peng, Q.; Du, S.; Shi, E.; Wu, S.; Li, Z.; Li, P.; Cao, A., *ACS Nano* **2013,** *7*, 8128-8135.

[15] Prasad, D.; Zhiling, L.; Satish, N.; Barrera, E. V., *Nanotechnology* **2004,** *15*, 379.

[16] Montazeri, M.; Fickenscher, M.; Smith, L. M.; Jackson, H. E.; Yarrison-Rice, J.; Kang, J. H.; Gao, Q.; Tan, H. H.; Jagadish, C.; Guo, Y.; Zou, J.; Pistol, M.-E.; Pryor, C. E., *Nano Lett.* **2010,** *10*, 880-886.

[17] Xu, F.; Durham, J. W.; Wiley, B. J.; Zhu, Y., *ACS Nano* **2011,** *5*, 1556-1563.

[18] Long, W.; Kenneth, J. L.; Wei-Hung, C.; Kausik, M., *Nanotechnology* **2018,** *29*, 105503.

[19] Ranjbartoreh, A. R.; Wang, B.; Shen, X.; Wang, G., *J. Appl. Phys.* **2011,** *109*, 014306.

[20] Novoselov, K. S.; Jiang, D.; Schedin, F.; Booth, T. J.; Khotkevich, V. V.; Morozov, S. V.; Geim, A. K., *Proc. Natl. Acad. Sci. U. S. A.* **2005,** *102*, 10451-10453.

[21] Reina, A.; Jia, X.; Ho, J.; Nezich, D.; Son, H.; Bulovic, V.; Dresselhaus, M. S.; Kong, J., *Nano Lett.* **2009,** *9*, 30-35.

[22] Liu, N.; Kim, P.; Kim, J. H.; Ye, J. H.; Kim, S.; Lee, C. J., *ACS Nano* **2014,** *8*, 6902-6910.

[23] Shuai, H.; Ge, P.; Hong, W.; Li, S.; Hu, J.; Hou, H.; Zou, G.; Ji, X., *Small Methods* **2019,** *0*, 1800328.

[24] Su, C.-Y.; Lu, A.-Y.; Xu, Y.; Chen, F.-R.; Khlobystov, A. N.; Li, L.-J., *ACS Nano* **2011,** *5*, 2332-2339.

[25] Li, D.; Kaner, R. B., *Science* **2008,** *320*, 1170-1171.

[26] Hernandez, Y., *Nat. Nanotech.* **2008,** *3*, 563–568.

[27] Hu, K.; Tolentino, L. S.; Kulkarni, D. D.; Ye, C.; Kumar, S.; Tsukruk, V. V., *Angew. Chem., Int. Ed.* **2013,** *52*, 13784-13788.

[28] Niu, L.; Coleman, J. N.; Zhang, H.; Shin, H.; Chhowalla, M.; Zheng, Z., *Small* **2016,** *12*, 272-293.

[29] Manna, K.; Hsieh, C.-Y.; Lo, S.-C.; Li, Y.-S.; Huang, H.-N.; Chiang, W.-H., *Carbon* **2016,** *105*, 551-555.

[30] Coleman, J. N., *Acc.Chem. Res.* **2013,** *46*, 14-22.

[31] Halim, U.; Zheng, C. R.; Chen, Y.; Lin, Z.; Jiang, S.; Cheng, R.; Huang, Y.; Duan, X., *Nat. Commun.* **2013,** *4*, 2213.

[32] Coleman, J. N.; Lotya, M.; O'Neill, A.; Bergin, S. D.; King, P. J.; Khan, U.; Young, K.; Gaucher, A.; De, S.; Smith, R. J.; Shvets, I. V.; Arora, S. K.; Stanton, G.; Kim, H.-Y.;

Lee, K.; Kim, G. T.; Duesberg, G. S.; Hallam, T.; Boland, J. J.; Wang, J. J.; Donegan, J. F.; Grunlan, J. C.; Moriarty, G.; Shmeliov, A.; Nicholls, R. J.; Perkins, J. M.; Grieveson, E. M.; Theuwissen, K.; McComb, D. W.; Nellist, P. D.; Nicolosi, V., *Science* **2011,** *331*, 568-571.

[33] Bracamonte, M. V.; Lacconi, G. I.; Urreta, S. E.; Foa Torres, L. E. F., *J. Phys. Chem. C* **2014,** *118*, 15455-15459.

[34] Park, S.; An, J.; Jung, I.; Piner, R. D.; An, S. J.; Li, X.; Velamakanni, A.; Ruoff, R. S., *Nano Lett.* **2009,** *9*, 1593-1597.

[35] Gupta, A.; Arunachalam, V.; Vasudevan, S., *J. Phys. Chem. Lett.* **2016,** *7*, 4884-4890.

[36] Jawaid, A.; Nepal, D.; Park, K.; Jespersen, M.; Qualley, A.; Mirau, P.; Drummy, L. F.; Vaia, R. A., *Chem. Mater.* **2016,** *28*, 337-348.

[37] Manna, K.; Huang, H.-N.; Li, W.-T.; Ho, Y.-H.; Chiang, W.-H., *Chem. Mater.* **2016,** *28*, 7586-7593.

[38] Li, Y.-S.; Liao, J.-L.; Wang, S.-Y.; Chiang, W.-H., *Sci. Rep.* **2016,** *6*, 22755.

[39] Cancado, L. G.; Pimenta, M. A.; Neves, B. R. A.; Dantas, M. S. S.; Jorio, A., *Phys. Rev. Lett.* **2004,** *93*, 247401.

[40] Malard, L. M.; Pimenta, M. A.; Dresselhaus, G.; Dresselhaus, M. S., *Phys. Rep.* **2009,** *473*, 51-87.

[41] Eckmann, A.; Felten, A.; Mishchenko, A.; Britnell, L.; Krupke, R.; Novoselov, K. S.; Casiraghi, C., *Nano Lett.* **2012,** *12*, 3925-3930.

[42] Ferrari, A. C.; Meyer, J. C.; Scardaci, V.; Casiraghi, C.; Lazzeri, M.; Mauri, F.; Piscanec, S.; Jiang, D.; Novoselov, K. S.; Roth, S.; Geim, A. K., *Phys. Review Lett.* **2006,** *97*, 187401.

[43] Tuinstra, F.; Koenig, J. L., *J. Chem. Phys.***1970,** *53*, 1126-1130.

[44] Yang, C.-R.; Tseng, S.-F.; Chen, Y.-T., *Nanomaterials* **2018,** *8*, 802.

[45] Eckmann, A.; Felten, A.; Verzhbitskiy, I.; Davey, R.; Casiraghi, C., *Phys. Rev. B* **2013,** *88*, 035426.

[46] Che, J.; Shen, L.; Xiao, Y., *J. Mater. Chem.* **2010,** *20*, 1722-1727.

[47] Chua, C. K.; Ambrosi, A.; Pumera, M., *J. Mater. Chem.* **2012,** *22*, 11054-11061.

[48] Dubin, S.; Gilje, S.; Wang, K.; Tung, V. C.; Cha, K.; Hall, A. S.; Farrar, J.; Varshneya, R.; Yang, Y.; Kaner, R. B., *ACS Nano* **2010,** *4*, 3845-3852.

[49] Lee, S. W.; Mattevi, C.; Chhowalla, M.; Sankaran, R. M., *J. Phys. Chem. Lett.* **2012,** *3*, 772-777.

[50] Pham, V. H.; Hur, S. H.; Kim, E. J.; Kim, B. S.; Chung, J. S., *Chem. Commun.* **2013,** *49*, 6665-6667.

[51] Pham, V. H.; Pham, H. D.; Dang, T. T.; Hur, S. H.; Kim, E. J.; Kong, B. S.; Kim, S.; Chung, J. S., *J. Mater. Chem.* **2012,** *22*, 10530-10536.

[52] Stankovich, S.; Dikin, D. A.; Piner, R. D.; Kohlhaas, K. A.; Kleinhammes, A.; Jia, Y.; Wu, Y.; Nguyen, S. T.; Ruoff, R. S., *Carbon* **2007,** *45*, 1558-1565.

[53] Tien, H. N.; Luan, V. H.; Lee, T. K.; Kong, B.-S.; Chung, J. S.; Kim, E. J.; Hur, S. H., *Chem. Eng. J.* **2012,** *211-212*, 97-103.

[54] Choi, K.; Eom, T.-J.; Lee, C., *Thin Solid Films* **2003,** *435*, 227-231.

[55] Shinozaki, A.; Arima, K.; Morita, M.; Kojima, I.; Azuma, Y., *Anal. Sci.* **2003,** *19*, 1557-1559.

[56] Harris, H. G.; Sabnis, G., *Structural modeling and experimental techniques*. CRC press: **1999**.

[57] Yu, T.; Ni, Z.; Du, C.; You, Y.; Wang, Y.; Shen, Z., *J. Phys. Chem. C* **2008,** *112*, 12602-12605.

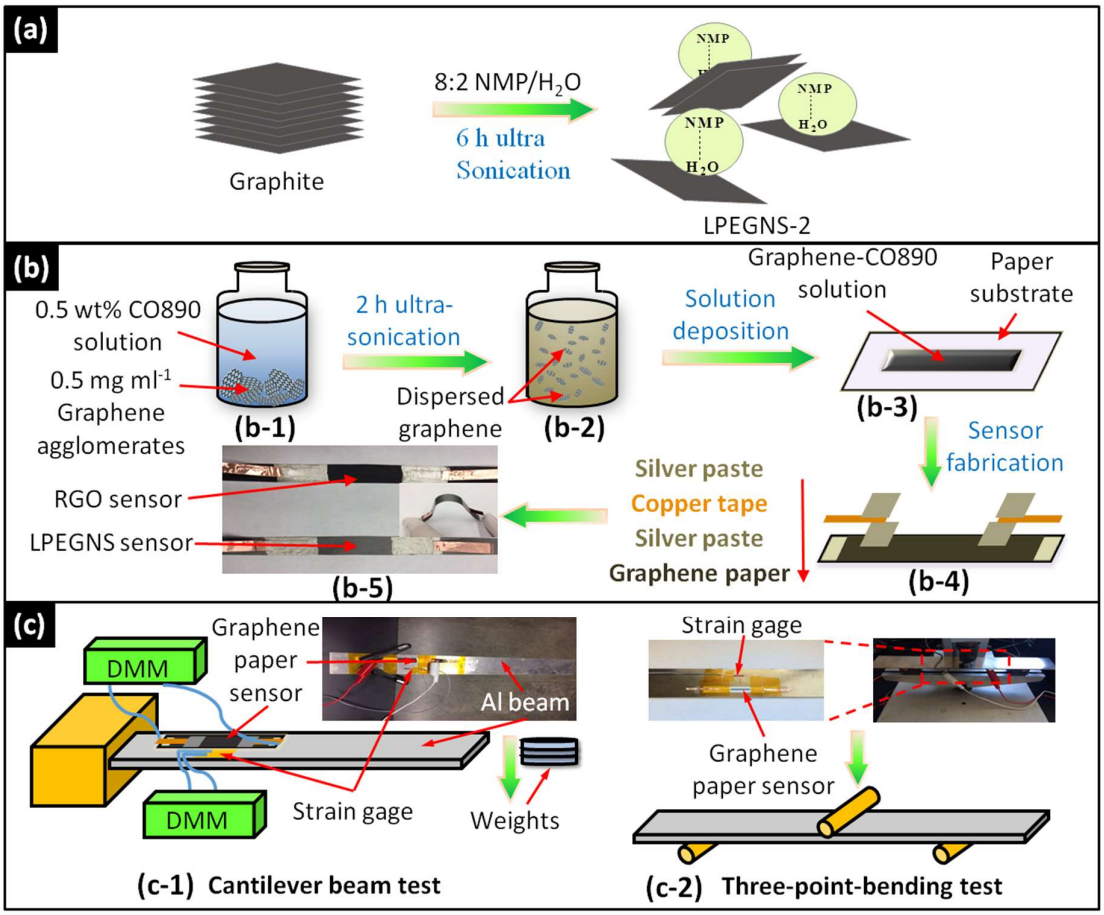

Figure1. (a) LPEGNS-2 was prepared from bulk graphite powder by a surfactant-free LPE using water as the co-solvent with NMP. (b) The graphene paper strain sensors were fabricated using a multi-step solution-based process. (b-1) graphene nanosheets were dispersed by subjecting graphene and CO890 solution mixture to (b-2) 2 h of ultrasonication. (b-3) Sonicated solution was uniformly deposited on printer paper. (b-4) Electrodes were established on both ends of completely dried specimens. (b-5) A photograph of an assembled RGO-CO890 and LPEGNR-2-CO890 (light grey) paper sensor are shown; the inset shows the graphene paper sensor was highly flexible. (c-1) A graphene paper sensor and a foil strain gage were both affixed onto an Al cantilevered beam, whose electrical resistances were measured using digital multimeters (DMM). The inset is a photograph of the test setup. Quasi-static strain was applied by loading the free-end of the beam using weights. (c-2) Schematic illustration of three-point-bending tests; the left and right insets show the backside of the steel plate and when it was loaded in the load frame, respectively.

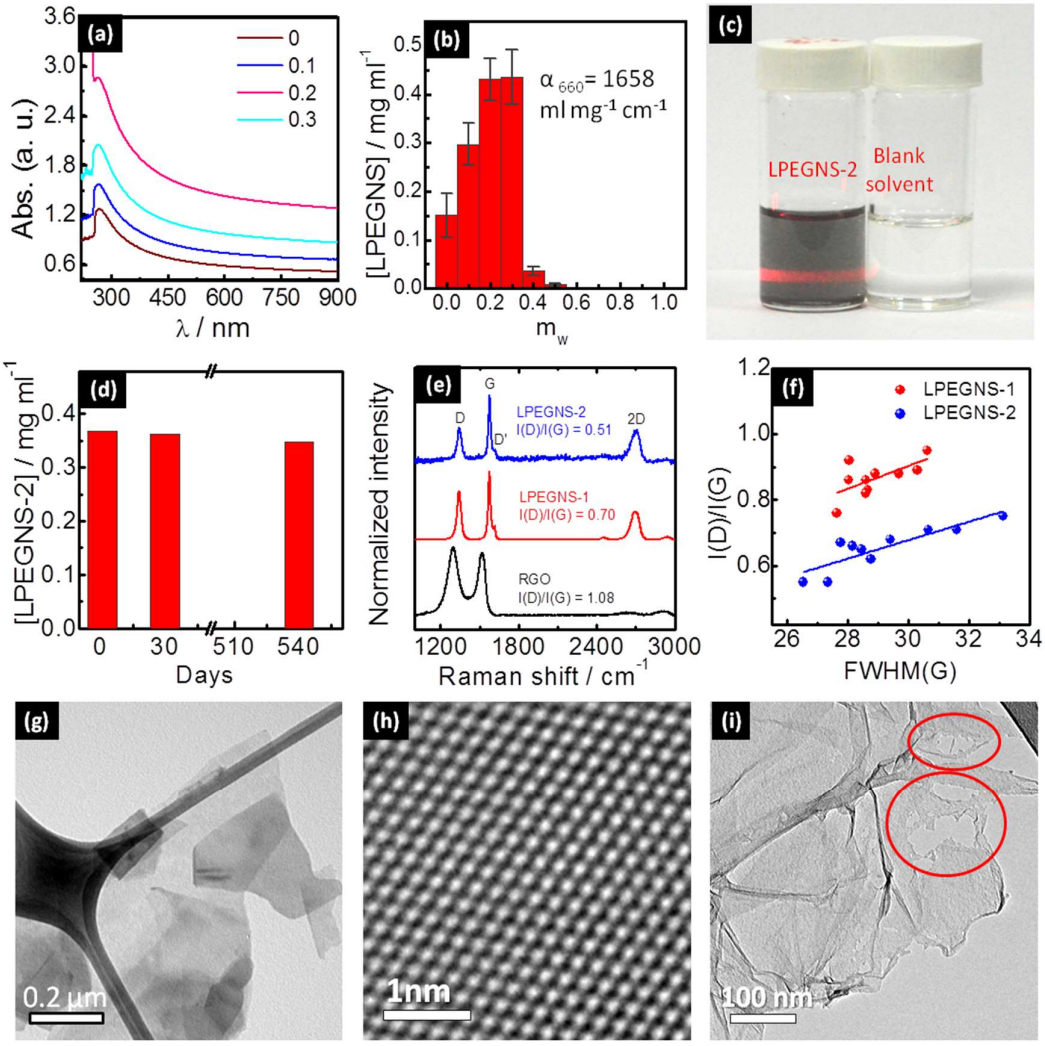

Figure 2. (a) UV-visible spectra and (b) concentration profiles of LPEGNS dispersion in NMP-water mixed solvent show m_w-dependent behavior. (c) An LPEGNS-2 colloidal dispersion (three-times diluted) generates the Tyndall effect even after 18 months from its preparation, and this is referenced to the pristine solvent of 8:2 NMP/H_2O. (d) The concentration profile of LPEGNS-2 dispersion as function of time. For (a), (b), and (d), all the absorption spectra were recorded using six-time diluted graphene dispersions, whereas, the concentrations of exfoliated dispersions are original. (e) Raman spectra of LPEGNS and RGO. (f) I(D)/I(G) versus FWHM(G) profiles of LPEGNS show statistically significant differences. (g) TEM and (h) HRTEM images of LPEGNS-2. (i) TEM image of RGO, the red circles show defects caused by oxidation.

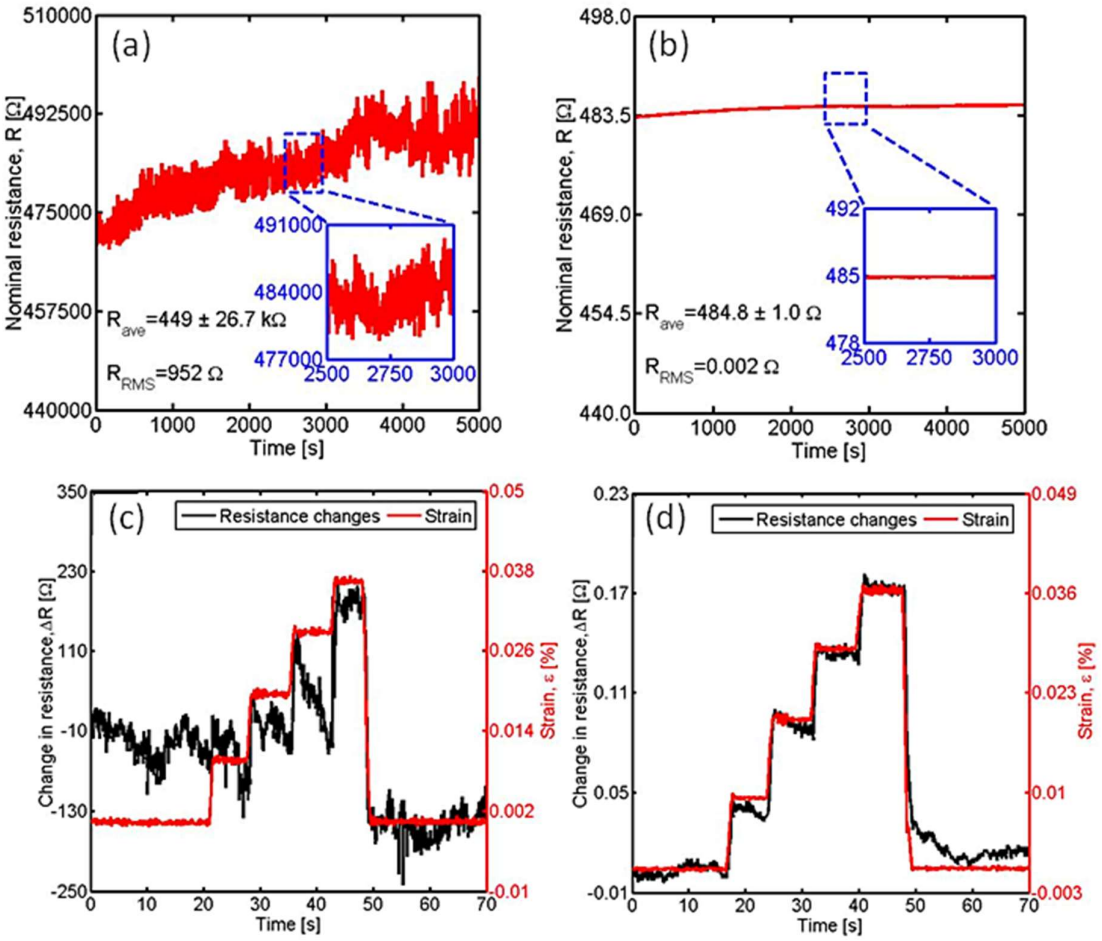

Figure 3. Representative unstrained nominal resistance time histories of (a) RGO-CO890 and (b) LPEGNS-2-CO890 paper sensors are shown. The corresponding insets show closer examinations of resistance fluctuations over a 500-s window for evaluating noise floor. The electromechanical responses of an RGO- (c) and LPEGNS-2-CO890 paper sensor (d) are overlaid with the applied strain pattern (measured using the foil strain gage).

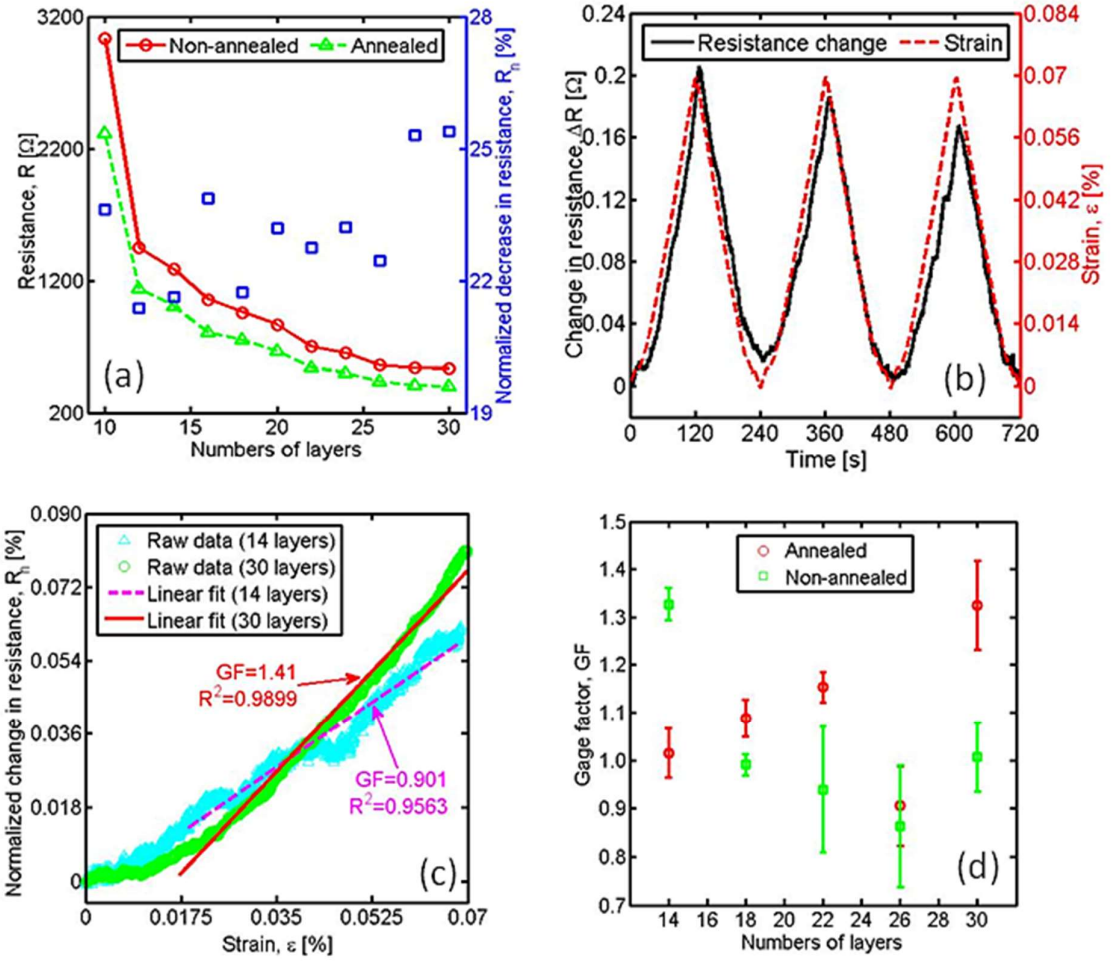

Figure 4. (a) Average nominal resistance of non-annealed and annealed LPEGNS-2-CO890 paper sensors was plotted with respect to the number of layers. The corresponding normalized decrease in resistance of all samples is also shown. (b) Representative resistance change of an annealed 30-layer LPEGNS-based sample when subjected to the three-point-bending test, which is overlapped with the applied strain pattern (acquired from strain gage). (c) Representative normalized resistance changes of an annealed 14- and 30-layer LPEGNS-based specimen during one loading cycle. The fitted least-square regression lines show well approximation of the actual responses. (d) The average GFs and their standard deviations (as error bars) of non-annealed and annealed LPEGNS-based paper sensors that were fabricated with different numbers of layers.

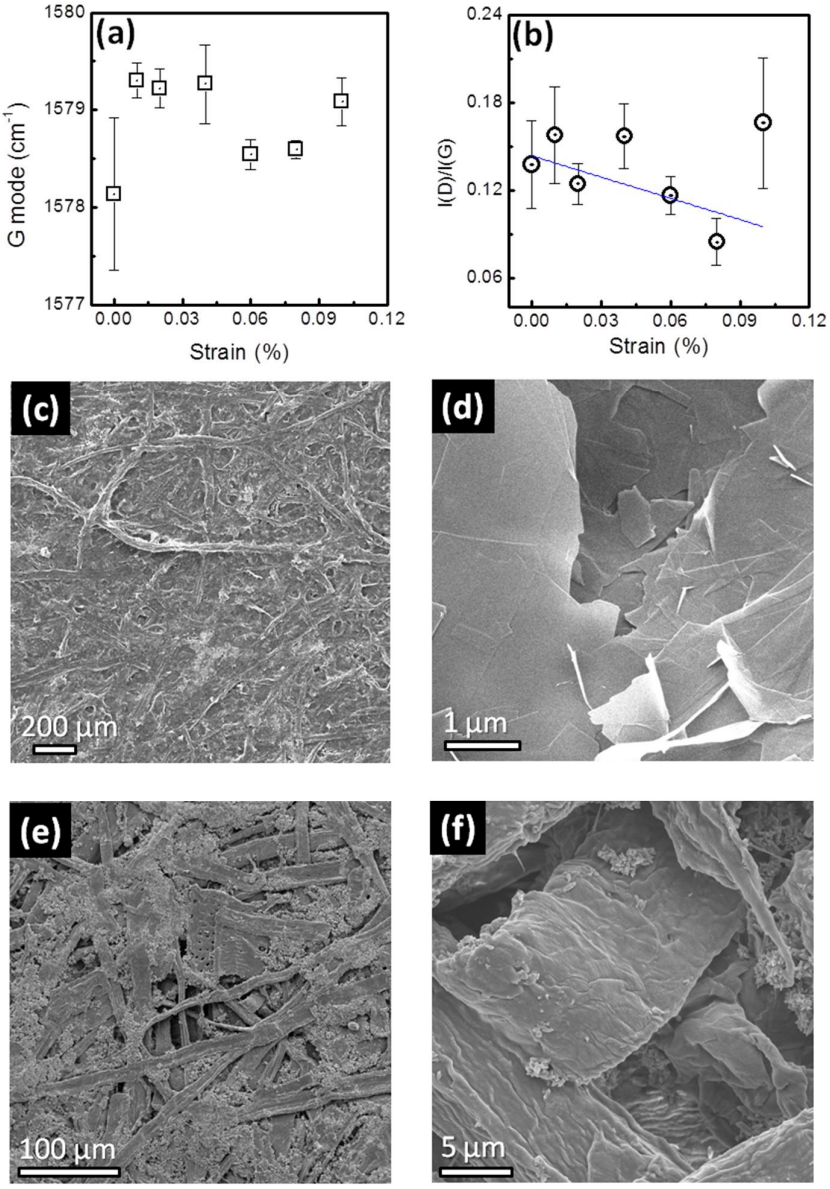

Figure 5. Effect of strain on the LPEGNS-2-CO890 on paper substrate. (a), (b) Raman spectroscopic analysis, (a) mean of the G mode frequency and (b) mean of I(D)/I(G) as fucntions of applied strain. The error bars are the standard deviations. (c) to (f) SEM images of LPEGNS-2-CO890 before strain (c),(d) and after 0.1 % strain (e), (f).

Graphene nanosheets (GNS) are produced from graphite by a liquid phase exfoliation (LPE) using water-N-methylpyrrolidinone (NMP) co-solvent system. The present solvent system enhances the exfoliation and the stability of the GNS dispersion, thereby lowering the defects in the GNS. High-quality LPEGNS enabled the production of higher performance (signal-to-noise ratio, strain sensitivity, conductivity, and stability) as compared to the conventional RGO.

Keyword: liquid phase exfoliation, graphene nanosheet, strain sensor, thin film

Kausik Manna, Long Wang, Kenneth J. Loh, and Wei-Hung Chiang**

Printed Strain Sensors using Graphene Nanosheets Prepared by Water-Assisted Liquid Phase Exfoliation

((Supporting Information can be included here using this template))

Supporting Information

Printed Strain Sensors using Graphene Nanosheets Prepared by Water-Assisted Liquid Phase Exfoliation

Kausik Manna, Long Wang, Kenneth J. Loh, and Wei-Hung Chiang**

Section S1. UV-visible spectroscopy

At appropriate water mass fractions (m_w), black dispersions of LPEGNS (**Figure S1**) were obtained. Systematic UV-visible spectra of LPEGNS dispersions were recorded as functions of m_w. The concentration of the LPEGNS dispersions were evaluated by filtration and weighing method[1], which, from the absorbance values at 660 nm, allowed for the estimation of absorption coefficient, α, (at 660 nm [1]) to be 1658 mL mg^{-1} cm^{-1} for LPEGNS.

This leads to the measurement of dispersed concentrations using the Lambert–Beer law, $A/l = \alpha C$, where, A/l is the absorbance per cell length. The as-prepared LPEGNS dispersions were found to be highly stable for 18 months. The stability of the LPEGNS-2 dispersion as a function of time was examined by estimation of dispersion concentration using UV-visible absorption spectroscopy (**Figure 2d**).

Section S2. Micro Raman spectroscopy

The Raman spectra were recorded at 10 randomly selected spots on the specimen, which was deposited on a Si wafer. All measurements were performed at ambient temperature. The G peak was fitted with a Guassian function, and this was performed for all of the spectra to obtain FWHM(G); these fits exhibited an average $r^2 = 0.98$). The intensity ratios of I(D)/I(G) and I(D)/I(D') and Guassian fittings were obtained after a careful baseline correction.

Section S3. X-ray photoelectron spectroscopy (XPS)

XPS was performed on LPEGNS-2 (**Figs. S2a** and **S2b**) and bulk graphite powder using the same dispersing media (8:2 NMP/water). Graphite as well as LPEGNS-2 show a characteristic C(1s) peak at 286 eV (**Figure S2a** and **S2b**). The binding energy for graphitic carbon was found to be consistent with previous reports [1]. The XPS wide scan spectrum for LPEGNS-2 as well as graphite powder (**Figure S2b**) show peaks at 533 eV, which correspond to O(1s). The low intense oxygen peaks in LPEGNS-2 and graphite powder might have appeared due to exposure to air. To confirm this hypothesis, XPS wide scan spectrum of blank Si-wafer was recorded, and the results show a O(1s) peak at 533 eV along with a C(1s) peak at 285 eV. Previous studies showed that trace amounts of airborne volatile organic compounds could be adsorbed onto the surfaces of Si-SiO_2 [2, 3], graphite, and analogous materials [4] due to exposure to air. Overall, these results show that our method produced single and few layers of graphene nanosheets without any chemical modification. The peaks observed (**Figure S2a**) can be attributed to residual NMP trapped on the graphene surface[1]. This idea was confirmed by similar observation in the XPS analysis of bulk powder graphite, which were prepared as films by dispersing in the same solvent. We observed slight broadening of the peaks associated with graphitic C, which might be due to the intercalation of solvent molecules during drying of the films[1].

Section S4. Mechanism of the water-assisted liquid phase exfoliation

The stabilization of the exfoliated nanosheets of LMs is one of the challenging tasks in LPE. In mixed solvent systems the solvent-solvent interactions can play significant role in the exfoliation process of layered materials by iinfluencing the solvent-solute interactions. **Figure S7** represents the effect of solvents on the stabilization of exfoliated nanosheets by the formation of $(NMP.2H_2O)_n$ clathrate aggregates due to water-NMP hetero-association. The water-NMP hetero-association directly influence exfoliation by preventing the recombination of exfoliated layers and the bulky $(NMP.2H_2O)_n$ aggregates are able to provide inter-sheet repulsive forces and separate the nanosheets with non-overlapping Leonard-Jones (L-J) potentials (**Figure S7a**). On the other hand, at higher m_w (> 0.5), the excess water molecules undergo self association rather than hetero-association with NMP molecules. In this molecular arrangement, NMP molecules hide completely in water molecular network and cannot interact with hydrophobic LMs[5] (**Figure S7b**). Consequently, highly water rich region is unable to produce high liquid exfoliation of LMs due to adverse solid-liquid interaction and the disruption of $(NMP.2H_2O)_n$ aggregates. Previous studies suggested that aqueous surfactant solutions are better exfoliating agents at pre-micellar than post-micellar region[6]. At pre-micellar region the hydrophobic tails of surfactant molecules can interact with hydrophobic LMs and prevent the recombination of exfoliated nanosheets while at post-micellar region those hydrophobic tails hide inside the micells allowing exfoliated nanosheets overlap. In this context, it is rational to assume that, the $(NMP.2H_2O)_n$ aggregates formed act as the surfactant molecules at the pre-micellar region and the hydrophobic NMP molecules possibly interact directly with the hydrophobic LMs surface (**Figure S8**).

Table S1. Defect parameters of as-exfoliated LPEGNS-1 and LPEGNS-2 evaluated from micro Raman spectral data. Full width half maximum (FWHM) for G band, intensity ratio of D and G band (I(D)/I(G)) and intensity ratio of D and D' band (I(D)/I(D')). Raman spectra were recorded on random 10 spots on the sample deposited on Si wafer.

Sample spots	FWHM(G)	I(D)/I(G)	I(D)/I(D')
LPEGNS-1			
1	29.69	0.88	2.92
2	30.62	0.95	2.89
3	28.04	0.92	3.94
4	30.30	0.89	2.97
5	28.60	0.86	3.25
6	28.03	0.86	4.00
7	27.63	0.76	4.07
8	28.90	0.88	4.03
9	28.66	0.83	3.00
10	28.60	0.82	3.71
LPEGNS-2			
1	27.76	0.67	3.37
2	26.53	0.55	3.09
3	28.16	0.66	3.87
4	28.76	0.62	3.95
5	29.40	0.68	3.79
6	31.59	0.71	3.95
7	27.34	0.55	4.42
8	28.45	0.65	3.50
9	30.66	0.71	3.48
10	33.13	0.75	3.70

Table S2. C/O ratio analysis from C1s (at%) and O1s (at%) in X-ray Photoelectron Spectroscopy (XPS) of LPEGNS-2 as a function of m_w.

m_w	C1s (at%)	O1s (at%)	C/O
0	90.21	9.79	9.21
0.1	95.43	4.57	16.64
0.2	96.77	3.23	29.96
0.3	96.17	3.83	25.11
0.4	97.56	2.44	39.98
0.5	62.73	37.27	1.77
0.6	57.47	42.53	1.74
0.7	57.1	42.9	1.85
0.8	53.15	46.85	1.13
0.9	43.14	56.86	0.76
1	46.2	53.8	0.86

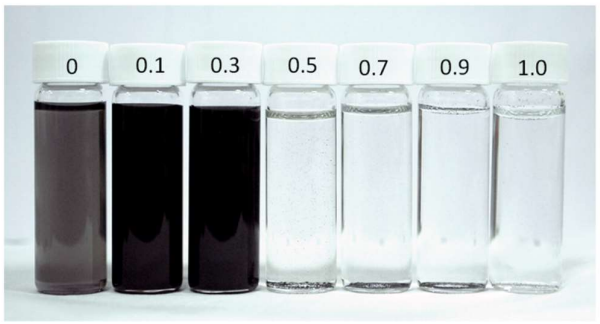

Figure S1. Photograph of GNS dispersions exfoliated in water-NMP mixed solvents. Different water mass fractions (m_w) are labeled on the corresponding vial in the figure.

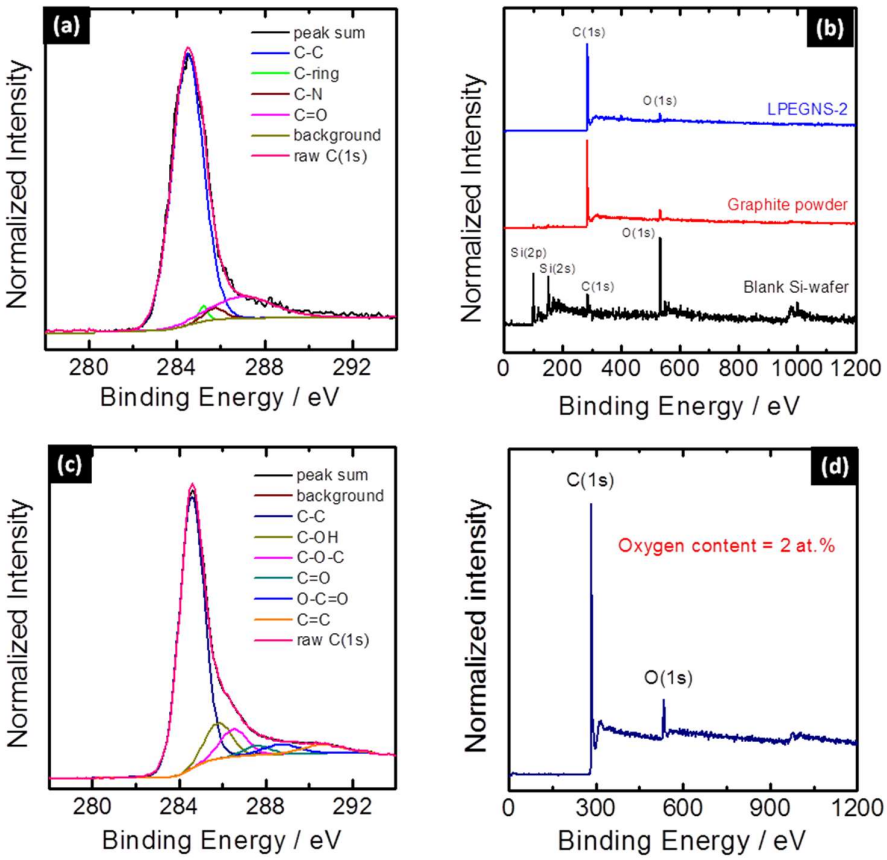

Figure S2. XPS of LPEGNS-2 (a) and RGO (c) with corresponding XPS wide scan spectra (b) and (d) respectively. The XPS wide scan spectrum of LPEGNS-2 is compared with that of graphite bulk powder and blank Si-wafer to observe the nature of the peak for oxygen.

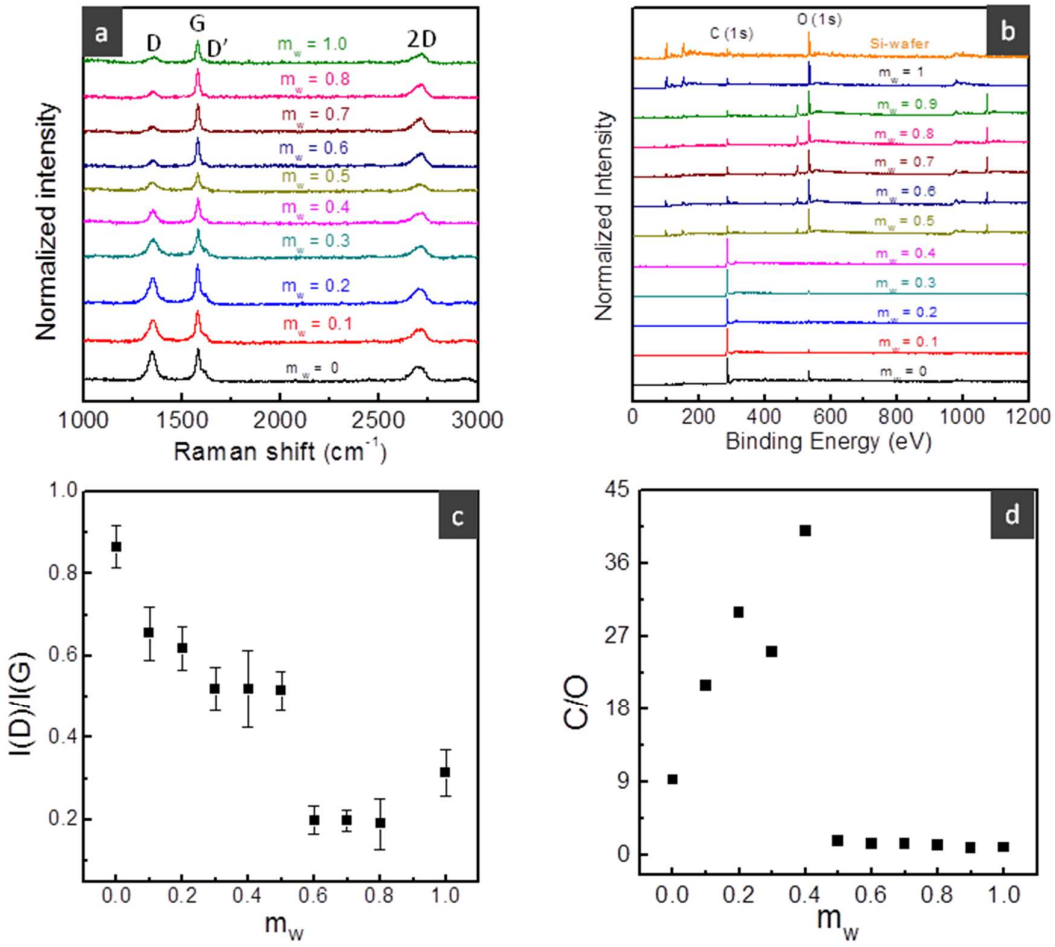

Figure S3. (a) Raman spectra, (b) wide scan XPS of LPEGNS as functions of m_w in water-NMP mixed solvent systems. The wide scan XPS of blank Si-wafer is also shown as reference. (c) I(D)/I(G) and (d) C/O ratio as obtained from XPS of LPEGNS for different water mass fractions (m_w). The error bars in (c) assign the standard deviations of I(D)/I(G) values

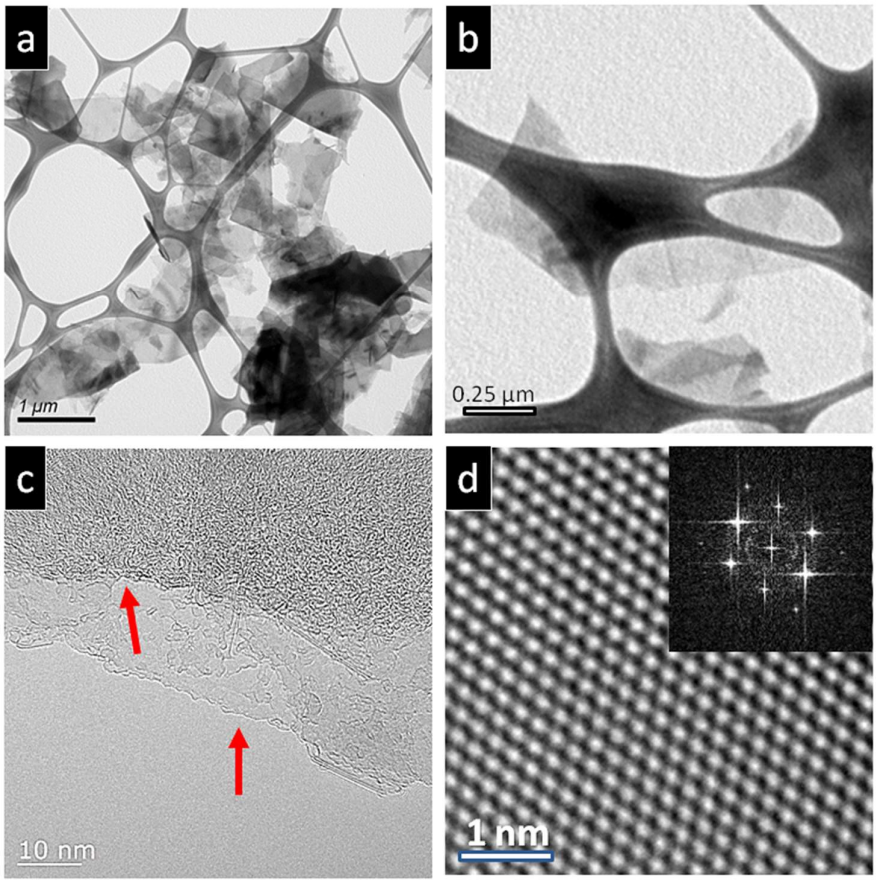

Figure S4. (a – c) TEM pictures, (d) HRTEM image and inset: corresponding fast Fourier transform (FFT) image of LPEGNS-2. The red arrows in (c) are showing the distinct layers of LPEGNS-2.

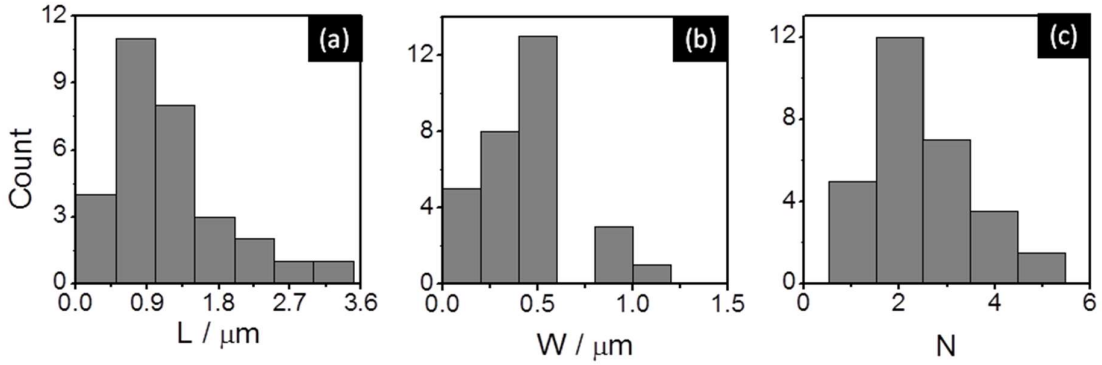

Figure S5. Statistical size analysis of LPEGNS-2. Here, L, W and N are the flake length, width and number of layer per nanosheets, respectively.

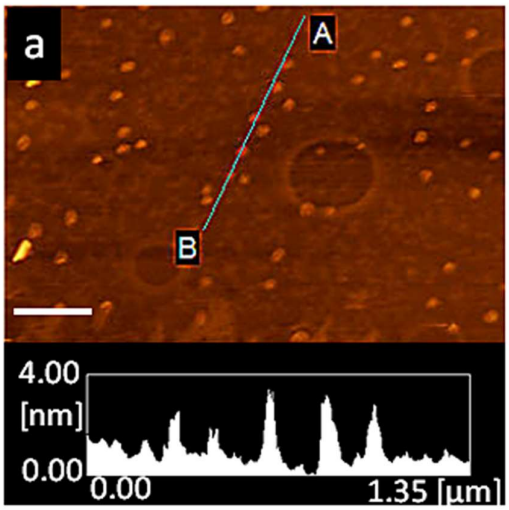

Figure S6. AFM image and section height profiles of LPEGNS-2

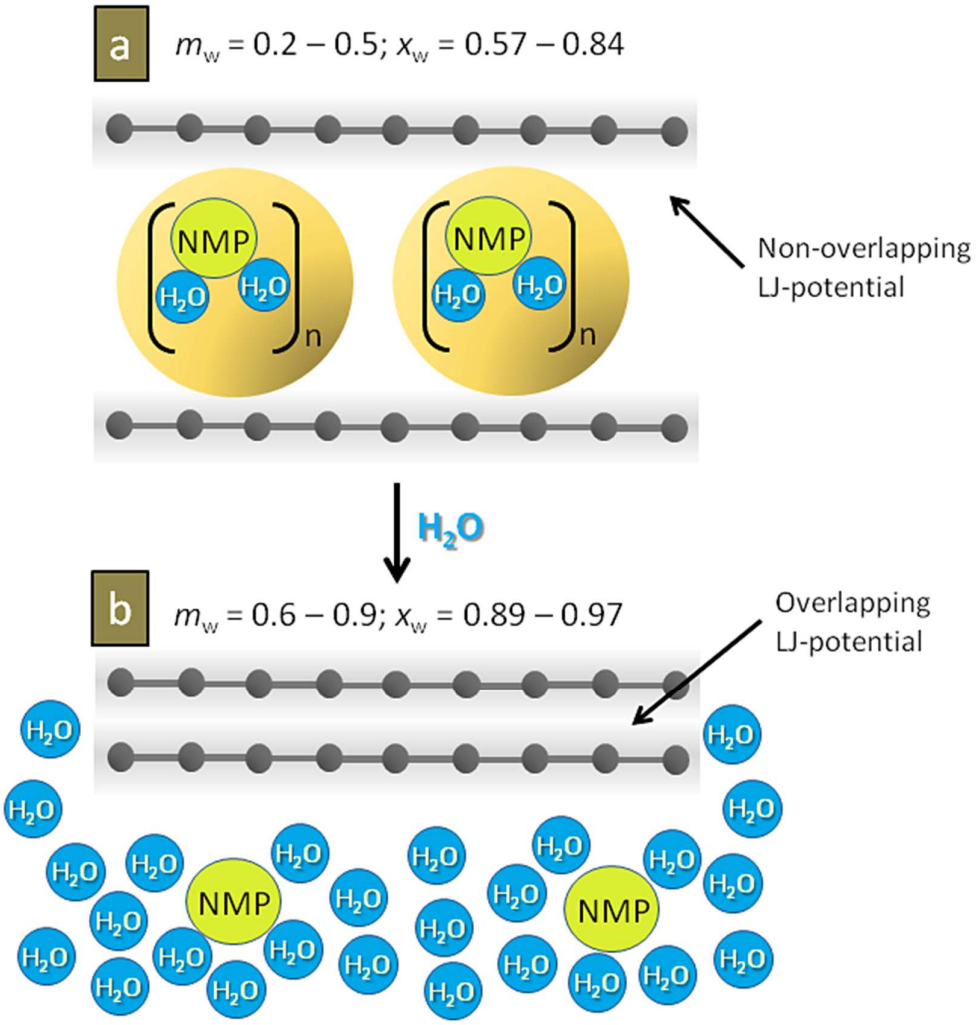

Figure S7. Schematic presentation of the effect of solvents on the stabilization of exfoliated materials. (a) The stabilization of the exfoliated nanosheets by $(NMP.2H_2O)_n$ aggregates formed by hetero-association between water and NMP molecules under favourable solid-liquid interaction preventing the Leonard-Jones interaction between exfoliated layers. (b) The overlapping of layers by Leonard-Jones interaction at highly water rich region due to the disruption of water-NMP aggregated structures and unfavourable solid-liquid interaction.

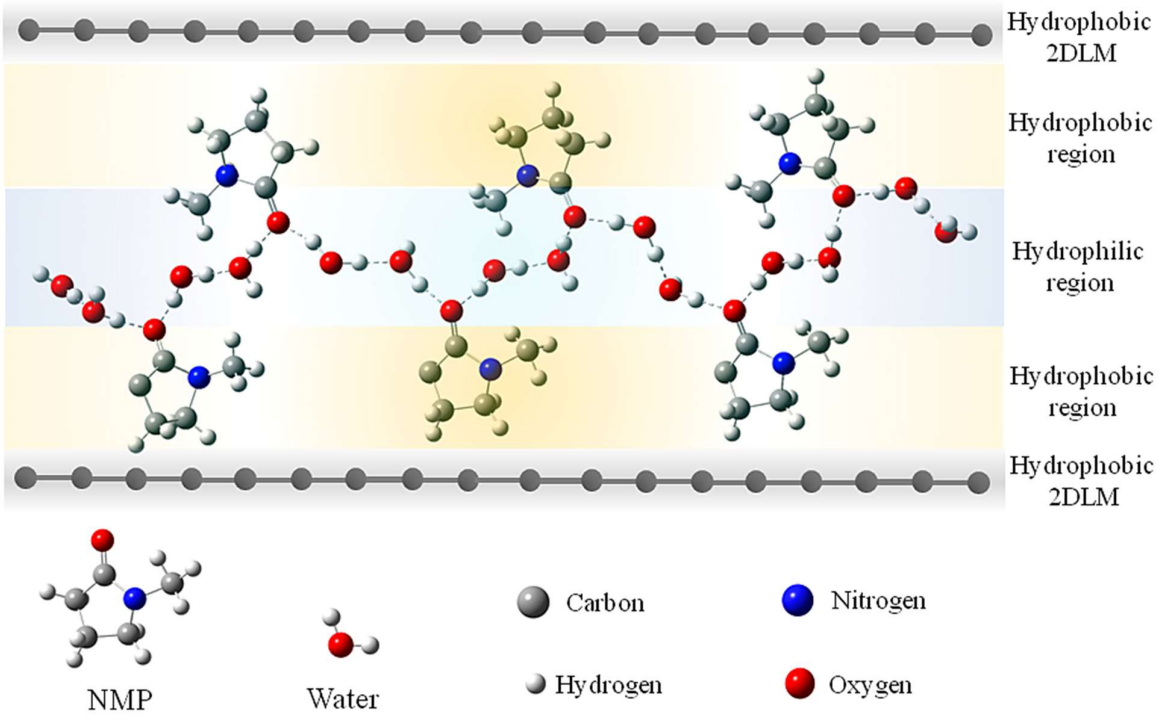

Figure S8. Hetero-association between water and NMP molecules at 2:1 mole ratio and formation of $(NMP.2H_2O)_n$ aggregates. The figure also schematically shows how the aggregates behave like amphiphilic molecules to create inter sheet repulsive force.

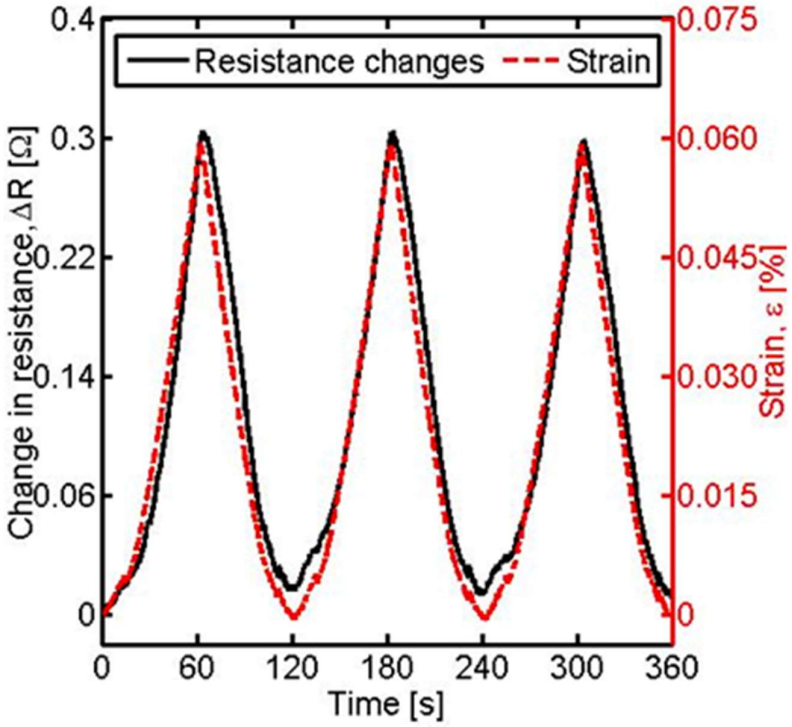

Figure S9. Representative resistance change of a non-annealed 30-layer LPEGNS-based sample when subjected to the three-point-bending test, which is overlapped with the applied strain pattern.

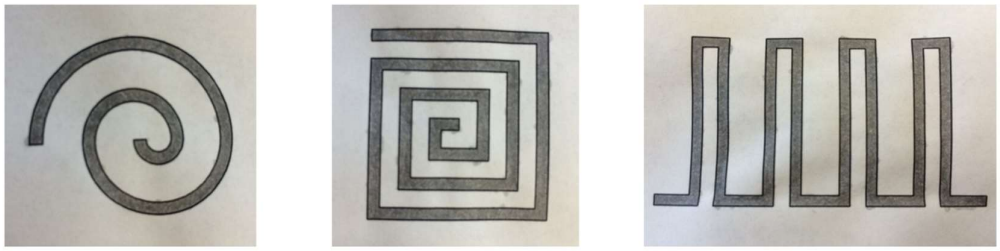

Figure S10. Different geometrical patterns were created by manually and selectively depositing 8 layers of GNS-CO890/ethanol solution on printer paper.

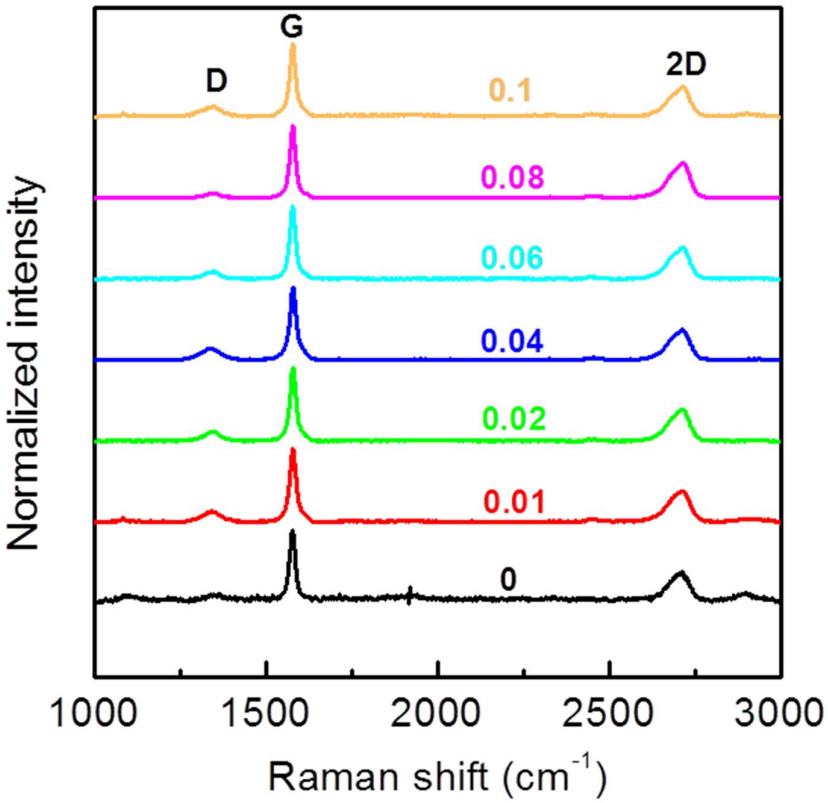

Figure S11. Representative *insitu* Raman spectra of LPEGNS-2-CO890 on paper substrate as functions of varying strain (mentioned in figure).

Reference

[1] Hernandez, Y., *Nat. Nanotech.* **2008,** *3*, 563–568.

[2] Choi, K.; Eom, T.-J.; Lee, C., *Thin Solid Films* **2003,** *435*, 227-231.

[3] Shinozaki, A.; Arima, K.; Morita, M.; Kojima, I.; Azuma, Y., *Analytical Sciences* **2003,** *19*, 1557-1559.

[4] Li, Z.; Wang, Y.; Kozbial, A.; Shenoy, G.; Zhou, F.; McGinley, R.; Ireland, P.; Morganstein, B.; Kunkel, A.; Surwade, S. P.; Li, L.; Liu, H., *Nat Mater* **2013,** *12*, 925-931.

[5] BRAITHWAITE, E. R., *Industrial Lubrication and Tribology* **1966,** *18*, 13-18.

[6] Lin, S.; Shih, C.-J.; Strano, M. S.; Blankschtein, D., *Journal of the American Chemical Society* **2011,** *133*, 12810-12823.

((Please insert your Supporting Information text/figures here. Please note: Supporting Display items, should be referred to as Figure S1, Equation S2, etc., in the main text…)